UNIVERSITY OF BIRMINGHAM

University of Birmingham Research at Birmingham

Detection of Solar-like Oscillations in Subgiant and Red Giant Stars Using 2 minute Cadence TESS Data

Zhou, Jianzhao; Bi, Shaolan; Yu, Jie; Li, Yaguang; Zhang, Xianfei; Li, Tanda; Long, Liu; Li, Mengjie; Sun, Tiancheng; Ye, Lifei

DOI:
10.3847/1538-4365/ad18db

License:
Creative Commons: Attribution (CC BY)

Document Version
Publisher's PDF, also known as Version of record

Citation for published version (Harvard):
Zhou, J, Bi, S, Yu, J, Li, Y, Zhang, X, Li, T, Long, L, Li, M, Sun, T & Ye, L 2024, 'Detection of Solar-like Oscillations in Subgiant and Red Giant Stars Using 2 minute Cadence TESS Data', *Astrophysical Journal. Supplement Series*, vol. 271, no. 1, 17. https://doi.org/10.3847/1538-4365/ad18db

Link to publication on Research at Birmingham portal

General rights
Unless a licence is specified above, all rights (including copyright and moral rights) in this document are retained by the authors and/or the copyright holders. The express permission of the copyright holder must be obtained for any use of this material other than for purposes permitted by law.

•Users may freely distribute the URL that is used to identify this publication.
•Users may download and/or print one copy of the publication from the University of Birmingham research portal for the purpose of private study or non-commercial research.
•User may use extracts from the document in line with the concept of 'fair dealing' under the Copyright, Designs and Patents Act 1988 (?)
•Users may not further distribute the material nor use it for the purposes of commercial gain.

Where a licence is displayed above, please note the terms and conditions of the licence govern your use of this document.

When citing, please reference the published version.

Take down policy
While the University of Birmingham exercises care and attention in making items available there are rare occasions when an item has been uploaded in error or has been deemed to be commercially or otherwise sensitive.

If you believe that this is the case for this document, please contact UBIRA@lists.bham.ac.uk providing details and we will remove access to the work immediately and investigate.

Download date: 28. Apr. 2024

The Astrophysical Journal Supplement Series, 271:17 (8pp), 2024 March https://doi.org/10.3847/1538-4365/ad18db

Detection of Solar-like Oscillations in Subgiant and Red Giant Stars Using 2 minute Cadence TESS Data

Jianzhao Zhou[1,2], Shaolan Bi[1,2], Jie Yu[3,4,5,6], Yaguang Li[7,8], Xianfei Zhang[1,2], Tanda Li[1,2,9], Liu Long[1,2], Mengjie Li[1,2], Tiancheng Sun[1,2], and Lifei Ye[1,2]

[1] Institute for Frontiers in Astronomy and Astrophysics, Beijing Normal University, Beijing 102206, People's Republic of China; bisl@bnu.edu.cn
[2] Department of Astronomy, Beijing Normal University, Beijing 100875, People's Republic of China
[3] School of Computing, Australian National University, Acton, ACT 2601, Australia; jie.yu@h-its.org
[4] Research School of Astronomy & Astrophysics, Australian National University, Cotter Road, Weston, ACT 2611, Australia
[5] Heidelberg Institute for Theoretical Studies (HITS) gGmbH, Schloss-Wolfsbrunnenweg 35, 69118 Heidelberg, Germany
[6] Max-Planck-Institut für Sonnensystemforschung, Justus-von-Liebig-Weg 3, 37077 Göttingen, Germany
[7] Sydney Institute for Astronomy (SIfA), School of Physics, University of Sydney, NSW 2006, Australia
[8] Institute for Astronomy, University of Hawai'i, 2680 Woodlawn Drive, Honolulu, HI 96822, USA
[9] School of Physics and Astronomy, University of Birmingham, Edgbaston, Birmingham, B15 2TT, UK

Received 2023 October 18; revised 2023 December 14; accepted 2023 December 22; published 2024 February 22

Abstract

Based on all 2 minute cadence TESS light curves from Sector 1 to 60, we provide a catalog of 8651 solar-like oscillators, including frequency at maximum power ($\nu_{\max}$, with its median precision $\sigma = 5.39\%$), large frequency separation ($\Delta\nu$, $\sigma = 6.22\%$), and seismically derived masses, radii, and surface gravity values. In this sample, we have detected 2173 new oscillators and added 4373 new $\Delta\nu$ measurements. Our seismic parameters are consistent with those from Kepler, K2, and previous TESS data. The median fractional residual in $\nu_{\max}$ is 1.63%, with a scatter of 14.75%, and in $\Delta\nu$ it is 0.11%, with a scatter of 10.76%. We have detected 476 solar-like oscillators with $\nu_{\max}$ exceeding the Nyquist frequency of Kepler long-cadence data during the evolutionary phases of subgiants and the base of the red giant branch, which provide a valuable resource for understanding angular momentum transport.

Unified Astronomy Thesaurus concepts: Asteroseismology (73); Subgiant stars (1646); Red giant stars (1372); Light curves (918)

Supporting material: machine-readable tables

1. Introduction

Astroseismology, the study of stellar oscillations, offers a powerful tool to infer stellar interiors (e.g., Christensen-Dalsgaard 1984; Aerts et al. 2010). In recent decades, space missions such as CoRoT (Baglin et al. 2006; Auvergne et al. 2009), Kepler (Borucki et al. 2010), and K2 (Howell et al. 2014) have provided long-duration, high-quality photometry data, leading to a revolution in the study of solar-like oscillations. These missions enabled the study of solar-like oscillations in hundreds of main-sequence and subgiant stars (e.g., Chaplin et al. 2011b, 2014; Li et al. 2020; Mathur et al. 2022), as well as tens of thousands of red giants (e.g., Hekker et al. 2011; Stello et al. 2013; Huber et al. 2014; Mathur et al. 2016; Yu et al. 2016, 2018; Hon et al. 2019), revealing new aspects of stellar structure and evolution (e.g., Hekker & Christensen-Dalsgaard 2017; Aerts et al. 2019).

The NASA Transiting Exoplanet Survey Satellite (TESS) mission (Ricker et al. 2015) has provided an opportunity to study solar-like oscillations in stars across the entire sky. Previous studies have extensively used TESS data to characterize solar-like oscillators, with a primary focus on the continuous viewing zones (CVZs) near the ecliptic pole, due to them having the longest observation durations (Silva Aguirre et al. 2020; Mackereth et al. 2021; Hon et al. 2022; Stello et al. 2022). Hon et al. (2021) initially used deep-learning techniques to detect solar-like oscillations in red giants across the full sky in the first 2 yr of TESS full-frame images (Sectors 1 to 26), identifying about 158,000 giants with $\nu_{\max}$. Hatt et al. (2023) detected 4177 solar-like oscillators using both 2 minute and 20 s cadence data (Sectors 1 to 46), reporting $\nu_{\max}$ and $\Delta\nu$ estimates.

By the end of Sector 60, TESS had completed observations of both the north and south ecliptic hemispheres for the second time. More than half of the targets with 2 minute data had been observed in at least two sectors. Longer photometric time series provide higher-frequency resolution in the Fourier domain, leading to improved precision in asteroseismic measurements. In this work, we aim to perform a complete search for solar-like oscillators and provide their global seismic parameters using TESS 2 minute cadence data. In addition, by combining $T_{\rm eff}$ from the Gaia Data Release (DR) 3 Radial Velocity Spectrometer (RVS) survey (Recio-Blanco et al. 2023), we estimate stellar radii, masses, and surface gravity using the seismic scaling relations.

2. Data Selection

2.1. Preliminary Data Selection

We download all available 2 minute cadence light curves spanning Sectors 1 to 60 (MAST Team 2021) from the Mikulski Archive for Space Telescopes (MAST). These light curves were extracted and detrended by the TESS Science Processing Operations Center (SPOC) pipeline (Twicken et al. 2016; Jenkins 2020).

A sample of stars selected for oscillation detection is based on the effective temperature ($T_{\rm eff}$) and radius (R) values from the

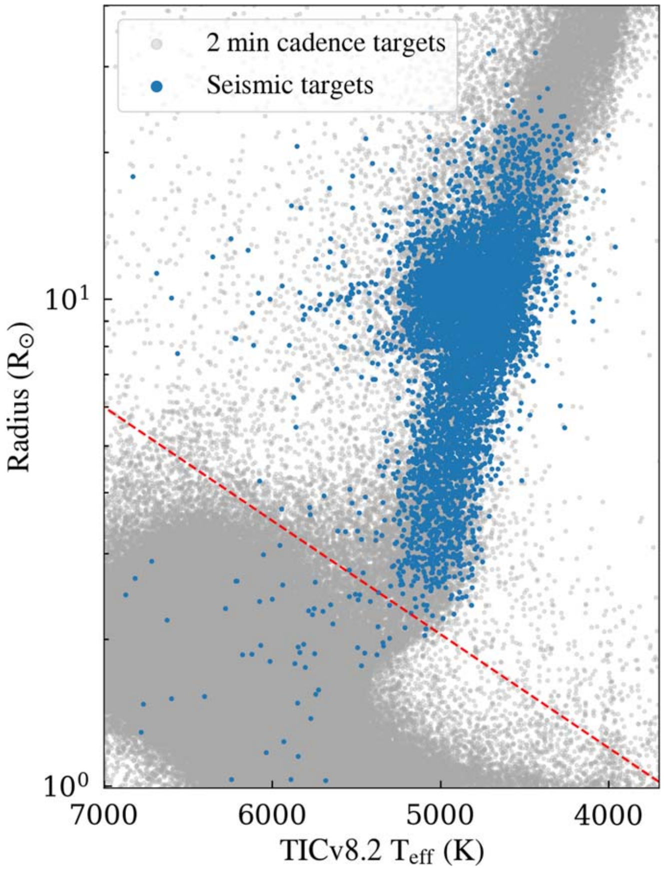

Figure 1. R vs. $T_{\rm eff}$ for 2 minute cadence targets and seismic targets. The $T_{\rm eff}$ and radii are sourced from TICv8.2. The light gray dots show the 2 minute cadence targets, the blue dots show the seismic targets, and the red dashed line, in reference to Hon et al. (2019), shows the boundary used to distinguish early subgiant stars from those ascending the red giant branch.

TESS Input Catalog version 8.2 (TICv8.2; Stassun et al. 2019), with criteria of $1\,R_\odot \leqslant R \leqslant 40\,R_\odot$ and $3700\,{\rm K} \leqslant T_{\rm eff} \leqslant 7000\,{\rm K}$. This resulted in the identification of 193,020 candidates, depicted as the gray dots in Figure 1. To categorize the stars into dwarfs and giants, we employ the relation $R = 10^p R_\odot$, with $p = \left(\frac{T_{\rm eff}({\rm K})}{7000} - \frac{3}{7}\right)\log\left(\frac{300}{7}\right) + \log(0.7)$ proposed by Hon et al. (2019) as the boundary (indicated by the red dashed line in Figure 1). This categorization results in 154,817 main-sequence stars and subgiants, as well as 38,203 red giants.

2.2. Seismic Data Detection

We transform all the light curves (PDCSAP data) of our preselected stars (Section 2.1) into power density spectra using the Lomb–Scargle periodogram method (VanderPlas 2018). We apply a 5σ clipping to remove outliers and divide the light curves by a 10 day median filter to eliminate low-frequency signals in each sector, and concatenate the light curves of all available sectors (García et al. 2011).

We detect the oscillation power excess in each power density spectrum using the collapsed autocorrelation function (collapsed ACF) method (Huber et al. 2009). First, we divide the power spectrum into equal logarithmic bins and smooth the result using an empirical 40% percentile filter to obtain a crude estimate of the background. Second, the residual power spectrum, obtained from dividing the power density spectrum by the estimated background, is segmented into overlapping subsets. The width of each subset is approximately $4\Delta\nu_{\rm exp}$ around its central frequency ($\nu_{\rm center}$), where $\Delta\nu_{\rm exp}$ is estimated as $0.263 \times \nu_{\rm center}^{0.772}$ (Stello et al. 2009). For each subset, we calculate the absolute ACF and then collapse the ACF by its referring $\nu_{\rm center}$. Finally, we smooth the collapsed ACFs with an empirical 7 μHz filter and fit them with a Gaussian profile centered on their maximum peak, along with constant noise.

We retain stars with a signal-to-noise ratio (S/N) greater than 1.5 and identify 7870 solar-like oscillators. For stars with $1.2 \leqslant {\rm S/N} \leqslant 1.5$, we carefully visually inspect their power density spectra for the presence of power excess and confirm 209 oscillators. The 8080 solar-like oscillators are shown in Figure 1 (blue dots), including 61 main-sequence stars and subgiants, and 8019 red giants. This indicates a solar-like oscillation detection rate of approximately 20% in red giants. Furthermore, we repeat the same procedure for stars not presented in TICv8.2 and identify an additional 571 oscillators. In total, we have identified an asteroseismic sample of 8651 stars.

Figure 2 illustrates the distribution of the sample across the ecliptic celestial sphere, covering nearly the entire sky. TESS focused on a specific segment of the ecliptic during the fourth year, spanning from Sector 42 to 46, to coincide with the portion of the K2 observation zones. Consequently, some stars (green dots) were observed for two to three sectors near the ecliptic. In order to minimize the contamination from stray Earth- and moonlight, TESS boresights toward a latitude of +85° in some sectors, which leads to an incomplete coverage of the northern hemisphere at low latitudes. The black dashed circles within 20° of the northern and southern ecliptic poles represent the CVZs.

3. Measuring Global Seismic Parameters

3.1. Measuring the Frequency at Maximum Power

We use the center of the fitted Gaussian profile to the collapsed ACF (Section 2.2) as the initial $\nu_{\rm max,guess}$. To fit the power density spectrum, we employ a model that consists of a Gaussian envelope, three background Harvey components, and white noise (Chaplin et al. 2014):

$$P(\nu) = \eta(\nu)^2\left[\sum_{i}^{3}\frac{2\sqrt{2}\,a_i/\pi b_i}{1+(\nu/b_i)^4} + H_g \exp\frac{-(\nu-\nu_{\rm max})^2}{2\sigma^2}\right] + W_{\rm n}, \quad (1)$$

where $\eta(\nu) = {\rm sinc}(\pi\nu/2\nu_{\rm nyq})$ accounts for the frequency-dependent attenuation resulting from the observational signal discretization, and $\nu_{\rm nyq}$ is the Nyquist frequency (e.g., Chaplin et al. 2011a; Kallinger et al. 2014). For other parameters, a_i and b_i represent the rms and the characteristic frequency of the ith Harvey component, respectively. H_g, $\nu_{\rm max}$, and σ are the height, the central frequency, and the width of the Gaussian envelope, respectively. $W_{\rm n}$ corresponds to the contribution of white noise.

We estimate $\nu_{\rm max}$ and its uncertainty by Bayesian inference using Markov Chain Monte Carlo (MCMC) simulations (Foreman-Mackey et al. 2013). The initial fitting parameters for MCMC are from the maximum likelihood estimation (MLE) method[10] (Huber et al. 2009; Kallinger et al. 2010). The minimum number of steps for the MCMC estimation is 3000 and the maximum number of steps is 5000. The $\nu_{\rm max}$ is estimated as the

---

[10] The initial fitting parameters used in MLE are derived from $\nu_{\rm max,guess}$.

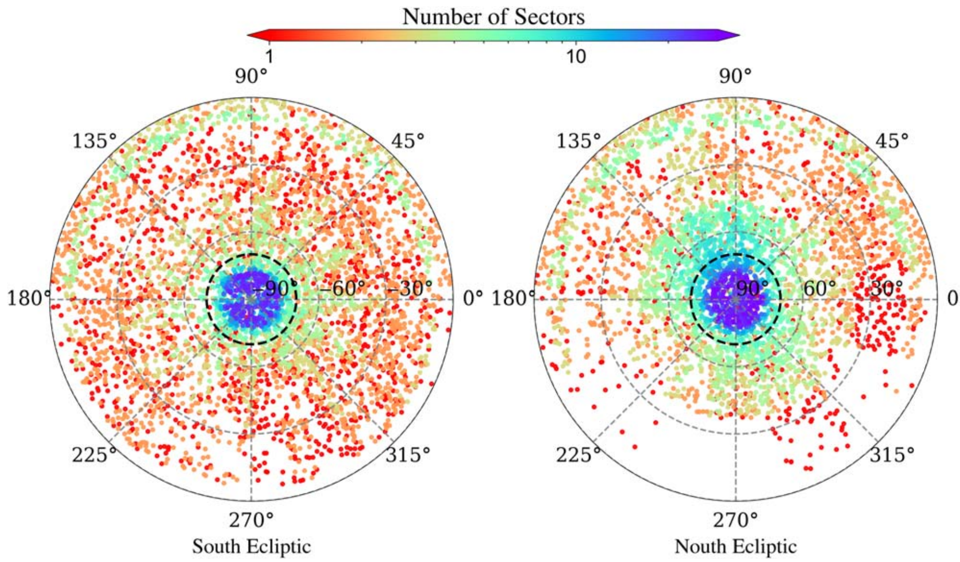

Figure 2. The distribution of detected solar-like oscillators across the celestial sphere. The color bar corresponds to the observation duration, denoted by the number of sectors. Some stars (green dots) are observed for two to three sectors near the ecliptic, because TESS focused on a specific segment of the ecliptic from Sector 42 to 46 coinciding with the portion of the K2 observation zones. The northern ecliptic hemisphere contains gaps to avoid excessive contamination from stray Earth- and moonlight, and the corresponding region appears at low latitudes close to the ecliptic. The black dashed circles represent the CVZs.

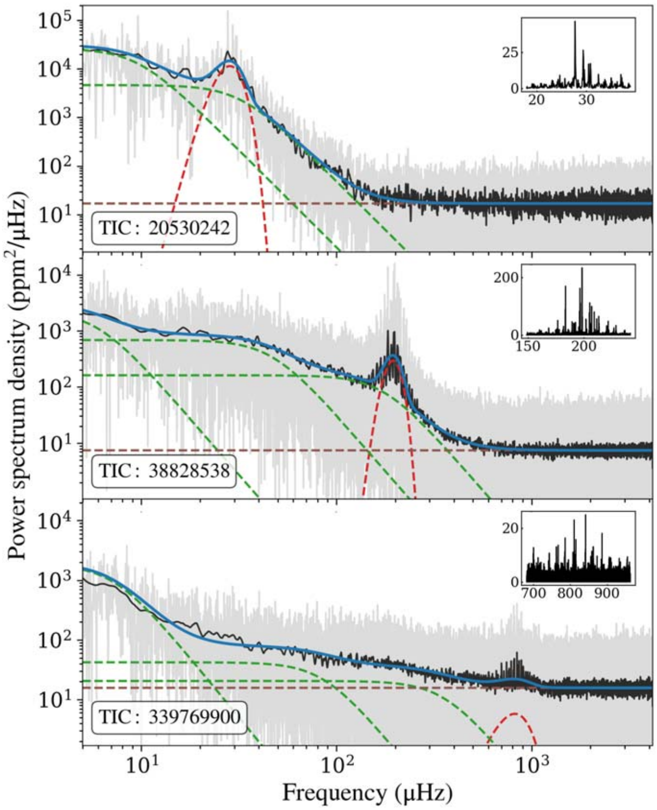

Figure 3. Representative power spectra of the TESS 2 minute cadence light curves. In each panel, the gray line shows the real data and the black line shows the data smoothed by a boxcar filter of 3 μHz wide. The solid blue line shows the MCMC fitting result, with the red dashed line for the fitted Gaussian envelope, the green dashed curve for the three Harvey components, and the brown straight line for the white noise. The inset figure shows the power spectrum near $\nu_{\rm max}$ divided by the background.

median of the posterior probability distribution, and the uncertainties are approximated as the 16th/84th percentiles. Representative examples of the background fitting are shown in Figure 3.

3.2. Measuring the Large Frequency Separation

We use the ACF method to measure the $\Delta\nu$ values (Huber et al. 2009; Chontos et al. 2022), shown in Figure 4. Figure 4(a) displays the échelle diagram of the oscillation modes. To prepare for the $\Delta\nu$ measurement, we first normalize the power density spectrum by dividing it by the MCMC-fitted background (Gaussian component excluded). Then we restrict the normalized power density spectrum to the frequency range of $\nu_{\rm max} \pm 3\Delta\nu_{\rm exp}$, as shown in Figure 4 (b). Within this frequency range, we calculate the ACF and apply a boxcar filter with an empirical width of $0.2\Delta\nu_{\rm exp}$. Finally, $\Delta\nu$ is measured as the maximum value within the range of 0.7–1.3 $\Delta\nu_{\rm exp}$ in the smoothed ACF, as depicted in Figure 4(c).

To evaluate the significance of the $\Delta\nu$ measurements, we calculate the S/N through dividing the maximum value of the normalized Fourier transforms (FTs) on the ACF by the noise, corresponding to half of $\Delta\nu$ or $\Delta\nu$. The noise is represented by the rms of the normalized FT on the ACF, as shown in Figure 4(d). Consequently, we obtain a sample of 7509 stars with valid $\Delta\nu$ measurements, adopting only $\Delta\nu$ measurements with $S/N \geqslant 3$.

Following Huber et al. (2011), the uncertainties of $\Delta\nu$ are estimated by conducting 500 perturbations on the power density spectrum using a χ^2 distribution with two degrees of freedom. For each perturbation, the fitting procedure is repeated, and the standard deviation of 500 measurements is considered as the uncertainty.

4. Results

4.1. Asteroseismic Sample

We present an asteroseismic sample of 8651 solar-like oscillators with $\nu_{\rm max}$, including 7509 stars with $\Delta\nu$. Notably, 2173 stars from this sample are new oscillators that were not previously detected (Hon et al. 2021, 2022; Hatt et al. 2023). Compared to Hatt et al. (2023), we add 4373 new $\Delta\nu$ for stars. Additionally, we flag 781 binaries and 85 exoplanet host stars by crossmatching the sample with the Spectroscopic Binary

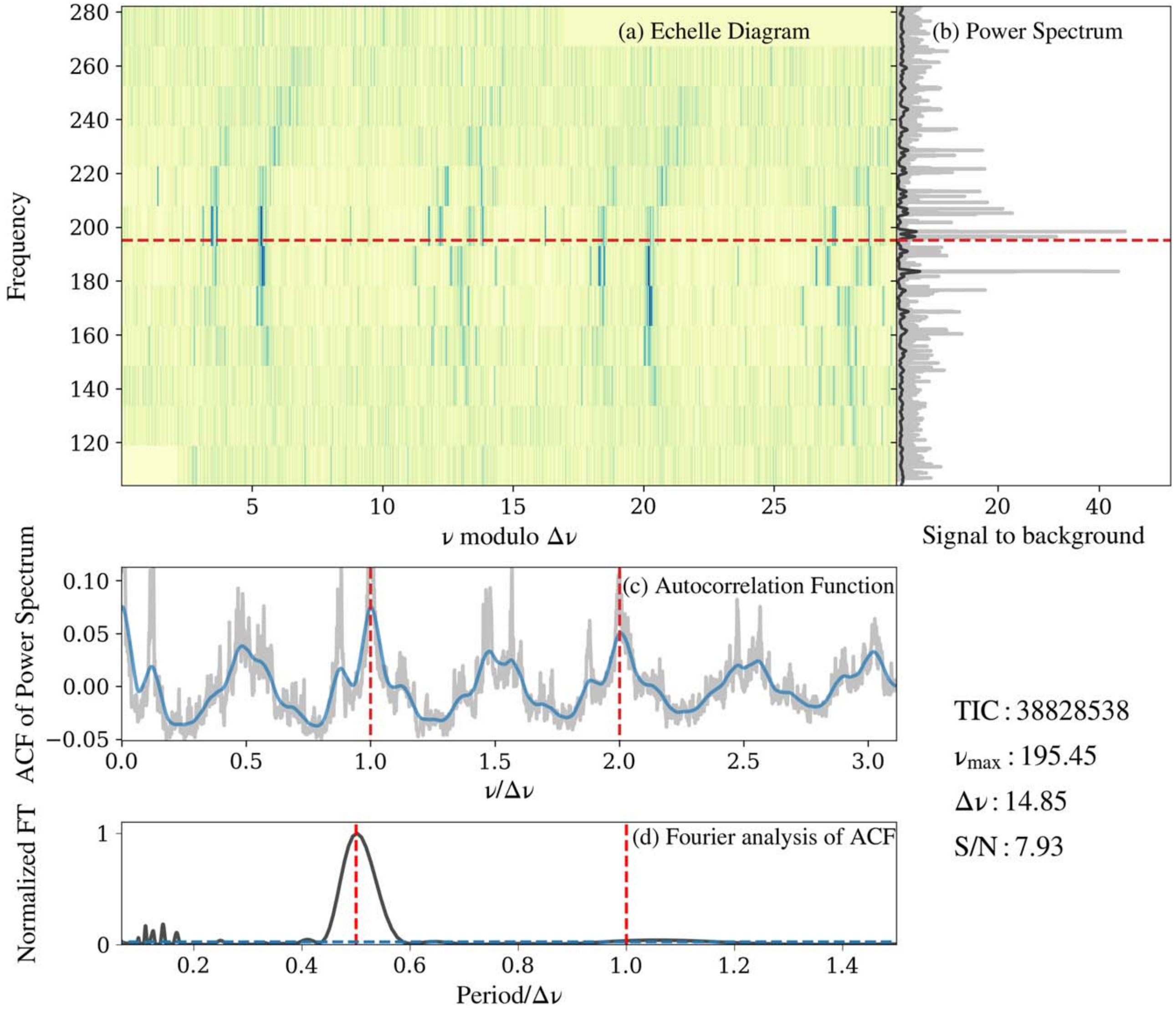

Figure 4. An example of measuring $\Delta\nu$ for TIC 38828538 (a) The échelle diagram—the red dashed line represents the value of $\nu_{\max}$. (b) The residual power spectrum. (c) The ACF—the two red dashed lines represent the positions of $\Delta\nu$ and twice $\Delta\nu$, from left to right. (d) The FTs of the ACF—the two red dashed lines represent the positions of half of $\Delta\nu$ and $\Delta\nu$ in period, from left to right, while the blue dashed line shows the noise.

Orbits Ninth Catalog,[11] the NASA Exoplanet Archive,[12] the TESS Eclipsing Binary Catalog,[13] and the Gaia DR3 `nss_two_body_orbit` Catalog, respectively (Pourbaix et al. 2004; Gaia Collaboration 2022 ; Howard et al. 2022; Prša et al. 2022). The results are listed in Table 1.

Figure 5 shows the histogram of the relative uncertainties for $\nu_{\max}$ and $\Delta\nu$. The number of sectors (N_{sectors}) marks the observation duration, with longer durations corresponding to lower uncertainties. This indicates that longer durations significantly improve measurement precision.

Figure 6 shows the well-established power-law relation of $\nu_{\max}$ and $\Delta\nu$ (Hekker et al. 2009; Stello et al. 2009). The black dotted line is expressed as $\Delta\nu = \alpha \cdot (\nu_{\max})^{\beta}$. It is fitted by an MCMC method, and consequently we obtain $\alpha = 0.236 \pm 0.001$ and $\beta = 0.789 \pm 0.001$. The $\nu_{\max}$ and $\Delta\nu$ exhibit a linear relation in logarithmic coordinates, especially for stars with $\sigma(\Delta\nu)/\Delta\nu \leqslant 0.1$. The stars having $\Delta\nu$ precision worse than 0.1 and $\nu_{\max} \sim$ 20–100 μHz may correspond to red clump stars, as they exhibit complex power spectra (Hon et al. 2017).

Figure 7 shows the histogram of the TESS magnitude (Tmag) for all 2 minute cadence stars and our sample. The number of our sample increases with Tmag at Tmag $<$ 5, which is consistent with the overall sample. However, for Tmag $>$ 9, the number of oscillators significantly decreases with increasing Tmag. This suggests an optimal magnitude range of $6 \leqslant \text{Tmag} \leqslant 9$ for observing solar-like oscillations. Additionally, there is a gap around Tmag = 7, consistent with Hatt et al. (2023). The gap exists in both all 2 minute cadence targets and our sample. We examined the histograms of Tmag for each sector from Sector 1 to 60 and found the gap in each of them. It possibly results from the inhomogeneous selection of TESS observations of 2 minute cadence data.

4.2. Comparison of $\nu_{\max}$ and $\Delta\nu$ Measurements

In Figure 8, we compare our global seismic parameters with those of common stars from the literature. The results demonstrate good agreement, despite the differences in the

---

[11] https://sb9.astro.ulb.ac.be/

[12] https://exoplanetarchive.ipac.caltech.edu/

[13] http://tessebs.villanova.edu/

Table 1
Stellar Global Oscillation Parameters

TIC	Tmag (mag)	$N_{\rm sectors}$	$\nu_{\rm max}$ (μHz)	$\sigma(\nu_{\rm max})$ (μHz)	$\Delta\nu$ (μHz)	$\sigma(\Delta\nu)$ (μHz)	S/N	Types	Source
1608	8.78	2	43.66	5.17	4.67	0.33	7.64	⋯	⋯
13727	7.31	1	188.99	5.04	16.91	0.94	7.39	⋯	⋯
80047	9.76	1	64.07	5.60	7.81	0.99	6.36	Binary	4
89696	8.63	1	43.13	1.84	4.81	0.57	3.71	⋯	⋯
92094	8.21	2	44.17	2.51	⋯	⋯	2.36	⋯	⋯
99433	4.42	2	73.55	5.20	⋯	⋯	2.82	⋯	⋯
105245	8.26	2	272.89	7.94	18.16	0.96	3.53	⋯	⋯
471011913	6.38	2	256.66	3.33	18.59	0.27	6.17	⋯	⋯
900749927	5.35	4	39.69	1.91	3.84	0.34	6.87	⋯	⋯

Note. The source of the adopted stellar type for each star is indicated by the following: (1) Spectroscopic Binary Orbits Ninth Catalog; (2) the TESS Eclipsing Binary Catalog; (3) NASA's Exoplanet Archive; and (4) the Gaia DR3 `nss_two_body_orbit` Catalog. S/N indicates the S/N of $\Delta\nu$.

(This table is available in its entirety in machine-readable form.)

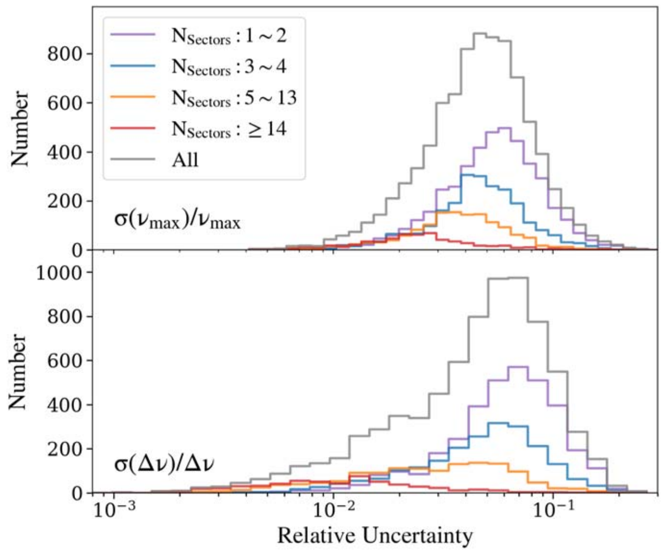

Figure 5. Histogram of relative uncertainties for $\nu_{\rm max}$ and $\Delta\nu$. $N_{\rm sectors}$ shows the number of sectors. The gray line represents the entire sample, while the purple, blue, yellow, and red lines represent stars observed for one to two sectors, three to four sectors, five to 13 sectors, and stars observed for more than 14 sectors, respectively.

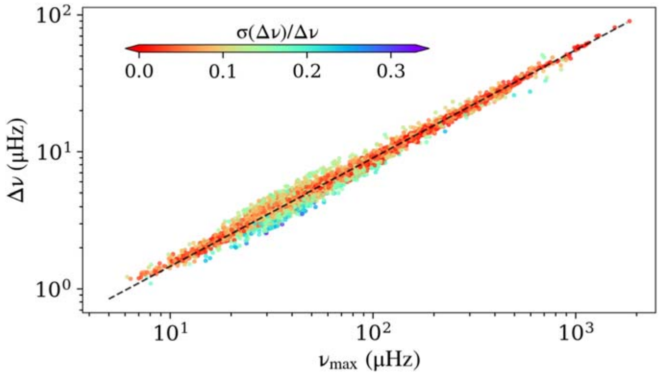

Figure 6. The relation of $\nu_{\rm max}$ and $\Delta\nu$ in logarithmic coordinates. The color bar shows the relative error of the measured $\Delta\nu$. The black dotted line follows an MCMC-fitted power-law relation: $\Delta\nu = \alpha\cdot(\nu_{\rm max})^{\beta}$, where $\alpha = 0.236 \pm 0.001$ and $\beta = 0.789 \pm 0.001$.

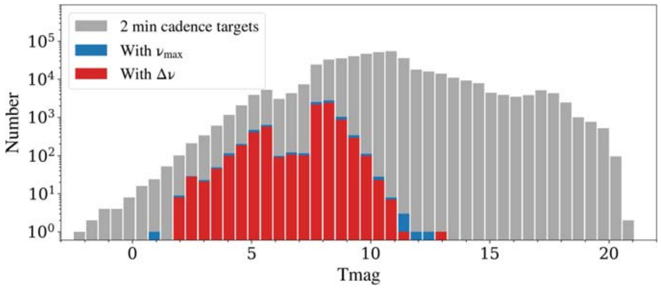

Figure 7. Histogram of Tmag for all 2 minute cadence targets and seismic stars. The gray color shows all 2 minute cadence targets, the blue color shows oscillators with $\nu_{\rm max}$, and the red color shows stars with $\Delta\nu$.

methods and data. The median fractional residual in $\nu_{\rm max}$ is 1.63%, with a scatter of 14.75%, while the median fractional residual in $\Delta\nu$ is 0.11%, with a scatter of 10.76%, as shown in Table 2.

Figure 9 shows the distribution in $\nu_{\rm max}$–$\nu_{\rm max}^{0.75}/\Delta\nu$ for our sample and stars in the Kepler/K2 long-cadence data and TESS 2 minute data from Hatt et al. (2023). Compared to the Kepler/K2 sample, on the one hand, there are fewer high-luminosity red giants in our sample, because our oscillators were observed within shorter duration. On the other hand, near the Nyquist frequency, it is possible to measure $\Delta\nu$ with long-cadence data, but challenging to measure $\nu_{\rm max}$, because the granulation background fitting could be biased and Nyquist aliases may occur (Yu et al. 2016, 2018). In this context, the TESS 2 minute cadence data prove valuable.

Notably, we have detected 401 solar-like oscillators with $\nu_{\rm max}$ exceeding the Nyquist frequency of the Kepler/K2 long-cadence data. These oscillators are more evolved subgiants or low-luminosity red giants, whose solar-like oscillations were seldom detected by either long- or short-cadence observations of the previous Kepler/K2 mission. Such stars transform from nearly uniform rotation to differential rotation, helping us to understand angular momentum transport (e.g., Aerts et al. 2019; Deheuvels et al. 2020; Kuszlewicz et al. 2023; Wilson et al. 2023).

4.3. Fundamental Stellar Parameters

By crossmatching our sample to Gaia DR3 RVS spectra data, we obtain 7173 stars with asteroseismic parameters and $T_{\rm eff}$. We estimate the radius ($R_{\rm seismic}$), mass ($M_{\rm seismic}$), and

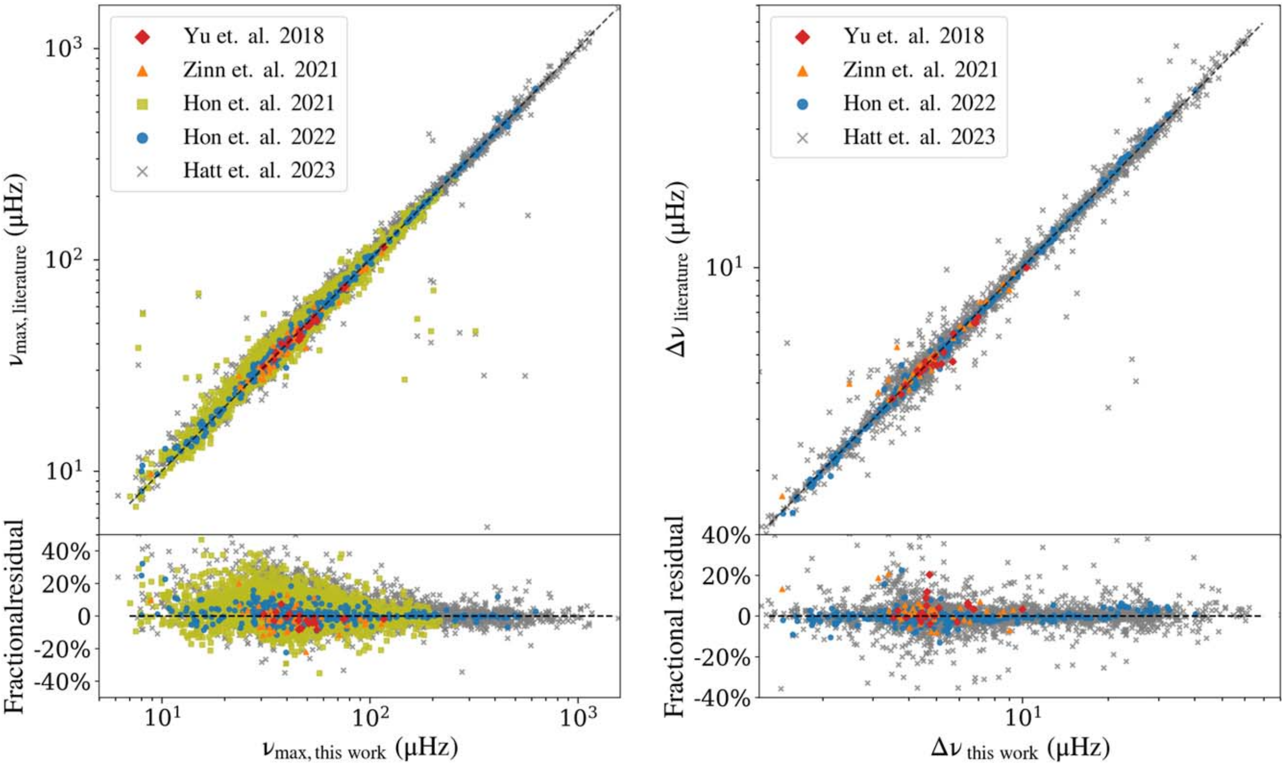

Figure 8. Comparison between the global seismic parameters measured in this work and those from previous literature. The black dashed lines in the top panel show the one-to-one relation between the two parameters. The bottom left panel shows the fractional residuals of $\nu_{\max}$, calculated as $(\nu_{\mathrm{max,literature}} - \nu_{\mathrm{max,this\ work}})/\nu_{\mathrm{max,\ this\ work}}$. Similarly, the bottom right panel displays the fractional residuals of $\Delta\nu$, calculated as $(\Delta\nu_{\mathrm{literature}} - \Delta\nu_{\mathrm{this\ work}})/\Delta\nu_{\mathrm{this\ work}}$.

Table 2
Comparison of Global Seismic Parameters with Previous Literature

Missions	Kepler	K2	TESS		
Cadences	30 minutes	30 minutes	30 minutes	30 minutes	120 and 20 s
Common Stars	20(1)	51(2)	5375(3)	348(4)	3129(5)
$\nu_{\max}$ Median Residual	−1.81%	−2.03%	1.37%	0.42%	2.49%
Scatter	3.63%	7.41%	13.53%	5.05%	17.21%
$\Delta\nu$ Median Residual	−1.99%	2.44%	…	−0.34%	0.11%
Scatter	4.88%	13.17%	…	3.68%	10.58%

Note. Common stars are sourced from: (1) Yu et al. (2018); (2) Zinn et al. (2019); (3) Hon et al. (2019); (4) Hon et al. (2021); and (5) Hatt et al. (2023).

surface gravity ($\log g$) of these stars by the scaling relations (Ulrich 1986; Brown et al. 1991; Kjeldsen & Bedding 1995; Belkacem et al. 2011)

$$\frac{M_{\mathrm{seismic}}}{M_{\odot}} \approx \left(\frac{\nu_{\max}}{\nu_{\max,\odot}}\right)^{3}\left(\frac{\Delta\nu}{\Delta\nu_{\odot}}\right)^{-4}\left(\frac{T_{\mathrm{eff}}}{T_{\mathrm{eff},\odot}}\right)^{3/2}, \tag{2}$$

$$\frac{R_{\mathrm{seismic}}}{R_{\odot}} \approx \left(\frac{\nu_{\max}}{\nu_{\max,\odot}}\right)\left(\frac{\Delta\nu}{\Delta\nu_{\odot}}\right)^{-2}\left(\frac{T_{\mathrm{eff}}}{T_{\mathrm{eff},\odot}}\right)^{1/2}, \tag{3}$$

$$\frac{g}{g_{\odot}} \approx \left(\frac{\nu_{\max}}{\nu_{\max,\odot}}\right)\left(\frac{T_{\mathrm{eff}}}{T_{\mathrm{eff},\odot}}\right)^{1/2}, \tag{4}$$

where $\nu_{\max,\odot} = 3090\ \mu$Hz, $\Delta\nu_{\odot} = 135.1\ \mu$Hz, and $T_{\mathrm{eff},\odot} =$ 5777 K, adopted from Huber et al. (2013). The estimates of M_{seismic}, R_{seismic}, and $\log g$ are listed in Table 3, with their median uncertainties of 9.20%, 6.24%, and 0.01 dex (0.79%), respectively.

To validate our asteroseimic radii, we use another independent method to derive radii and luminosities for these stars. We employ the SEDEX pipeline (Yu et al. 2021, 2023) alongside MARCS model spectra for performing the spectral energy distribution (SED) fitting. Our approach adopts spectroscopic T_{eff}, $\log g$, and [M/H] priors (from Gaia DR3 RVS spectra) and combines them with the apparent magnitudes from 32 bandpasses across nine photometric databases (Yu et al. 2023) to derive both extinction and bolometric fluxes. Leveraging Gaia DR3 parallaxes, we then compute the luminosities and deduce the stellar radii in conjunction with the spectroscopic T_{eff}. The uncertainties in bolometric fluxes are assessed through a Bayesian framework, and the uncertainties in luminosities and radii were determined via error propagation given the T_{eff} uncertainties. It is noted that the above two methods adopt the same effective temperature,

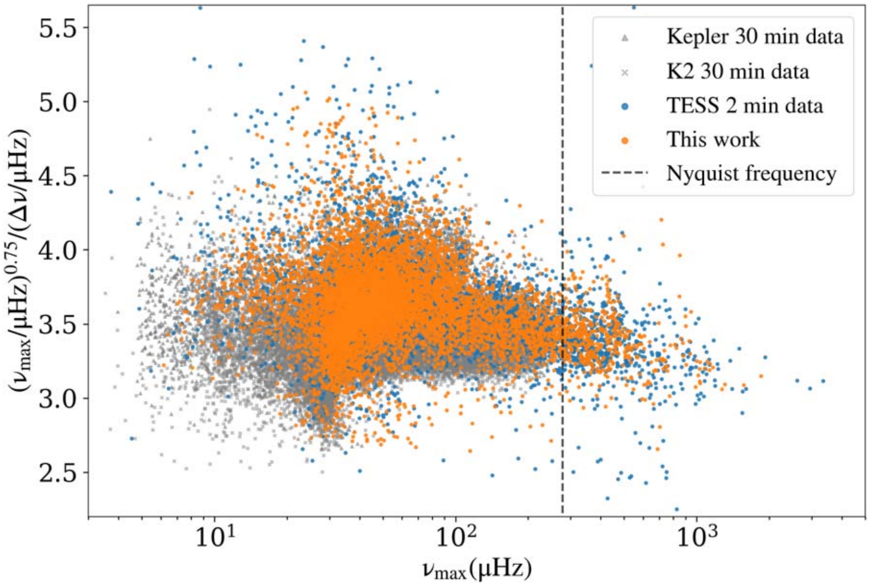

Figure 9. $\nu_{\max}$ vs. $\nu_{\max}^{0.75}/\Delta\nu$ diagram. The horizontal axis shows $\nu_{\max}$, while the vertical axis shows $\nu_{\max}^{0.75}/\Delta\nu$, which is a mass proxy related to temperature. The gray triangles and crosses represent samples from the Kepler and K2 long-cadence data, respectively. The blue dots show the sample from previous TESS 2 minute data, as presented by Hatt et al. (2023), and the yellow dots show our sample.

Table 3
Fundamental Stellar Parameters

TIC	T_{eff} (K)	$\log g$ (cgs)	M_{seismic} ($M_\odot$)	R_{seismic} ($R_\odot$)	R_{SED} ($R_\odot$)	L_{SED} $\log(L/L_\odot)$
1608	4739.0 ± 11.0	2.55 ± 0.03	1.47 ± 0.14	10.72 ± 0.19	11.09 ± 0.11	1.747 ± 0.016
13727	4795.0 ± 162.5	3.19 ± 1.89	0.71 ± 0.06	3.56 ± 0.23	4.02 ± 0.04	0.908 ± 0.040
80047	4736.0 ± 28.5	2.73 ± 0.09	0.60 ± 0.14	5.62 ± 0.89	6.52 ± 0.24	1.282 ± 0.035
89696	4768.0 ± 22.0	2.55 ± 0.04	1.27 ± 0.42	10.01 ± 1.88	8.81 ± 0.10	1.554 ± 0.016
11688264	4756.0 ± 10.0	2.20 ± 0.01	0.69 ± 0.32	10.95 ± 2.87	11.72 ± 0.11	1.801 ± 0.016
11738052	4854.0 ± 3.5	2.78 ± 0.02	1.12 ± 0.25	7.15 ± 1.04	8.58 ± 0.04	1.562 ± 0.015
12063724	4720.0 ± 11.5	2.56 ± 0.03	1.70 ± 0.20	11.40 ± 0.08	10.01 ± 0.07	1.651 ± 0.015
12333486	4677.0 ± 8.5	2.43 ± 0.02	1.82 ± 0.44	13.70 ± 1.93	13.08 ± 0.35	1.867 ± 0.027
12358786	4747.0 ± 10.0	2.69 ± 0.03	1.04 ± 0.08	7.70 ± 0.54	7.97 ± 0.07	1.464 ± 0.016
12376694	4595.0 ± 9.0	2.37 ± 0.02	0.71 ± 0.03	9.14 ± 0.40	10.77 ± 0.09	1.666 ± 0.015

Note. Catalog of fundamental stellar parameters for 7173 stars. T_{eff} values are collected from Gaia DR3 RVS spectra, the stellar M_{seismic}, R_{seismic}, and $\log g$ values are provided by scaling relations, and the R_{SED} and L_{SED} values are obtained through the SED fitting.

(This table is available in its entirety in machine-readable form.)

implying that the measurements in both approaches may be subject to potential systematic effects related to T_{eff}. Figure 10 shows the comparison between R_{seimic} and R_{SED}. The result reveals a good agreement, with a median fractional residual of −0.79% and a standard deviation of 16.60%. This consistency is partly attributed to employing the same effective temperature in both measurements. The estimates of R_{SED} and L_{SED} are also listed in Table 3.

5. Conclusions

We have presented a sample of 8651 solar-like oscillators with $\nu_{\max}$ measurements, including 7509 stars with $\Delta\nu$, using TESS 2 minute cadence light curves. Comparing with the literature, we have newly detected 2173 oscillators and added 4373 $\Delta\nu$ measurements. Our seismic parameters demonstrate good consistency with those from previous studies. The median fractional residual for $\nu_{\max}$ is 1.63%, with a scatter of 14.75%, and the median fractional residual for $\Delta\nu$ is 0.11%, with a scatter of 10.76%.

We have detected 476 solar-like oscillators that exhibit $\nu_{\max}$ values exceeding the Nyquist frequency of Kepler/K2 long-cadence data, which increases the sample size of more evolved subgiants and low-luminosity red giants. Such oscillators may provide observational constraints on the stellar internal rotation profiles, which potentially contributes to our understanding of angular momentum transport.

We have estimated asteroseismic masses (with a median precision of 9.21%), radii (with a median precision of 6.24%), and $\log g$ for a subset of 7173 stars crossmatched from Gaia DR3 RVS spectra data. Our asteroseismic radii are in good agreement with the radii from the SED fitting.

Our sample covers the entire sky, showing the advantage of the TESS mission in detecting solar-like oscillators. With further observations by TESS, a greater number and diversity of potential solar-like oscillators are expected to be detected. This will provide valuable observational targets for future missions, such as PLATO (to be launched in 2026), which will significantly improve observations of stars with detectable solar-like oscillations. A higher-precision sample of solar-like

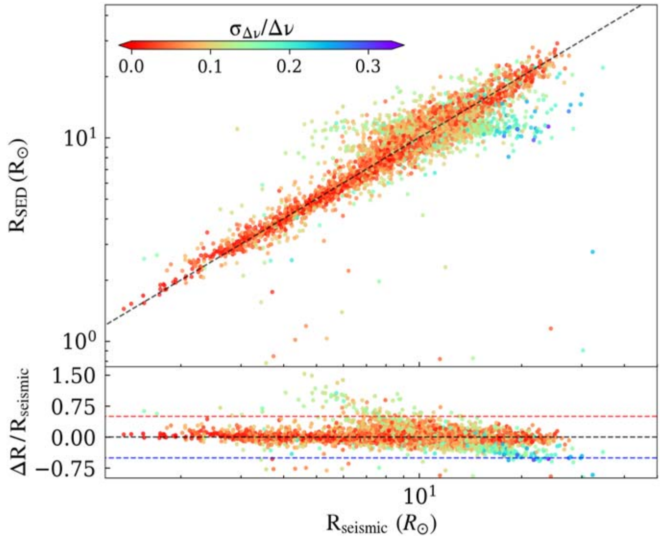

Figure 10. Comparisons of radii from the asteroseismic scaling relations with radii from the SED fitting. The color bar represents the relative error of $\Delta\nu$. The bottom panel displays the fractional residuals between radius estimates, denoted as $\Delta R = R_{\rm SED} - R_{\rm seismic}$.

oscillators spanning from main-sequence stars to red giants will provide new perspectives on stellar structure and evolution.

Acknowledgments

We thank Timothy R. Bedding, Ruijie Shi, and HuanYu Teng for helpful discussions. This work is supported by the Joint Research Fund in Astronomy (U2031203) under cooperative agreement between the National Natural Science Foundation of China (NSFC) and Chinese Academy of Sciences (CAS), and NSFC grants (12090040, 12090042, and 12073006). We also acknowledge the science research grant from the China Manned Space Project, with No. CMS-CSST-2021-A10, and the CSST project.

This paper includes data collected by the TESS mission. Funding for the TESS mission is provided by the NASA Explorer Program. Funding for the TESS Asteroseismic Science Operations Center is provided by the Danish National Research Foundation (grant agreement No. DNRF106), ESA PRODEX (PEA 4000119301), and the Stellar Astrophysics Centre (SAC) at Aarhus University. We acknowledge the use of public TESS data from pipelines at the TESS Science Office and at the TESS Science Processing Operations Center. Resources supporting this work were provided by the NASA High-End Computing (HEC) Program through the NASA Advanced Supercomputing (NAS) Division at the Ames Research Center for the production of the SPOC data products.

This work has made use of data from the European Space Agency (ESA) mission Gaia (https://www.cosmos.esa.int/gaia), processed by the Gaia Data Processing and Analysis Consortium (DPAC; https://www.cosmos.esa.int/web/gaia/dpac/consortium). Funding for the DPAC has been provided by national institutions, in particular the institutions participating in the Gaia Multilateral Agreement.

ORCID iDs

Jianzhao Zhou https://orcid.org/0009-0004-9024-9666
Shaolan Bi https://orcid.org/0000-0002-7642-7583
Jie Yu https://orcid.org/0000-0002-0007-6211
Yaguang Li https://orcid.org/0000-0003-3020-4437
Xianfei Zhang https://orcid.org/0000-0002-3672-2166
Tanda Li https://orcid.org/0000-0001-6396-2563
Liu Long https://orcid.org/0000-0003-2908-1492
Tiancheng Sun https://orcid.org/0000-0003-0795-4854
Lifei Ye https://orcid.org/0009-0009-1338-1045

References

Aerts, C., Christensen-Dalsgaard, J., & Kurtz, D. W. 2010, Asteroseismology (Dordrecht: Springer Netherlands)
Aerts, C., Mathis, S., & Rogers, T. M. 2019, ARA&A, 57, 35
Auvergne, M., Bodin, P., Boisnard, L., et al. 2009, A&A, 506, 411
Baglin, A., Auvergne, M., Boisnard, L., et al. 2006, in 36th COSPAR Scientific Assembly (Paris: COSPAR), 3749
Belkacem, K., Goupil, M. J., Dupret, M. A., et al. 2011, A&A, 530, A142
Borucki, W. J., Koch, D., Basri, G., et al. 2010, Sci, 327, 977
Brown, T. M., Gilliland, R. L., Noyes, R. W., & Ramsey, L. W. 1991, ApJ, 368, 599
Chaplin, W. J., Basu, S., Huber, D., et al. 2014, ApJS, 210, 1
Chaplin, W. J., Kjeldsen, H., Bedding, T. R., et al. 2011a, ApJ, 732, 54
Chaplin, W. J., Kjeldsen, H., Christensen-Dalsgaard, J., et al. 2011b, Sci, 332, 213
Chontos, A., Huber, D., Sayeed, M., & Yamsiri, P. 2022, JOSS, 7, 3331
Christensen-Dalsgaard, J. 1984, Space Research Prospects in Stellar Activity and Variability, ed. A. Mangeney & F. Praderie, 11
Deheuvels, S., Ballot, J., Eggenberger, P., et al. 2020, A&A, 641, A117
Foreman-Mackey, D., Hogg, D. W., Lang, D., & Goodman, J. 2013, PASP, 125, 306
Gaia Collaboration 2022, yCat, I/357
García, R. A., Hekker, S., Stello, D., et al. 2011, MNRAS, 414, L6
Hatt, E., Nielsen, M. B., Chaplin, W. J., et al. 2023, A&A, 669, A67
Hekker, S., & Christensen-Dalsgaard, J. 2017, A&ARv, 25, 1
Hekker, S., Gilliland, R. L., Elsworth, Y., et al. 2011, MNRAS, 414, 2594
Hekker, S., Kallinger, T., Baudin, F., et al. 2009, A&A, 506, 465
Hon, M., Huber, D., Kuszlewicz, J. S., et al. 2021, ApJ, 919, 131
Hon, M., Kuszlewicz, J. S., Huber, D., Stello, D., & Reyes, C. 2022, AJ, 164, 135
Hon, M., Stello, D., García, R. A., et al. 2019, MNRAS, 485, 5616
Hon, M., Stello, D., & Yu, J. 2017, MNRAS, 469, 4578
Howard, E. L., Davenport, J. R. A., & Covey, K. R. 2022, RNAAS, 6, 96
Howell, S. B., Sobeck, C., Haas, M., et al. 2014, PASP, 126, 398
Huber, D., Bedding, T. R., Stello, D., et al. 2011, ApJ, 743, 143
Huber, D., Chaplin, W. J., Christensen-Dalsgaard, J., et al. 2013, ApJ, 767, 127
Huber, D., Silva Aguirre, V., Matthews, J. M., et al. 2014, ApJS, 211, 2
Huber, D., Stello, D., Bedding, T. R., et al. 2009, CoAst, 160, 74
Jenkins, J. M. 2020, Kepler Data Processing Handbook KSCI-19081-003, NASA Ames Research Center
Kallinger, T., De Ridder, J., Hekker, S., et al. 2014, A&A, 570, A41
Kallinger, T., Mosser, B., Hekker, S., et al. 2010, A&A, 522, A1
Kjeldsen, H., & Bedding, T. R. 1995, A&A, 293, 87
Kuszlewicz, J. S., Hon, M., & Huber, D. 2023, ApJ, 954, 152
Li, Y., Bedding, T. R., Li, T., et al. 2020, MNRAS, 495, 2363
Mackereth, J. T., Miglio, A., Elsworth, Y., et al. 2021, MNRAS, 502, 1947
MAST Team 2021, TESS Light Curves - All Sectors, MAST, doi:10.17909/t9-nmc8-f686
Mathur, S., García, R. A., Breton, S., et al. 2022, A&A, 657, A31
Mathur, S., García, R. A., Huber, D., et al. 2016, ApJ, 827, 50
Pourbaix, D., Tokovinin, A. A., Batten, A. H., et al. 2004, A&A, 424, 727
Prša, A., Kochoska, A., Conroy, K. E., et al. 2022, ApJS, 258, 16
Recio-Blanco, A., de Laverny, P., Palicio, P. A., et al. 2023, A&A, 674, A29
Ricker, G. R., Winn, J. N., Vanderspek, R., et al. 2015, JATIS, 1, 014003
Silva Aguirre, V., Stello, D., Stokholm, A., et al. 2020, ApJL, 889, L34
Stassun, K. G., Oelkers, R. J., Paegert, M., et al. 2019, AJ, 158, 138
Stello, D., Chaplin, W. J., Basu, S., Elsworth, Y., & Bedding, T. R. 2009, MNRAS, 400, L80
Stello, D., Huber, D., Bedding, T. R., et al. 2013, ApJL, 765, L41
Stello, D., Saunders, N., Grunblatt, S., et al. 2022, MNRAS, 512, 1677
Twicken, J. D., Jenkins, J. M., Seader, S. E., et al. 2016, AJ, 152, 158
Ulrich, R. K. 1986, ApJL, 306, L37
VanderPlas, J. T. 2018, ApJS, 236, 16
Wilson, T. A., Casey, A. R., Mandel, I., et al. 2023, MNRAS, 521, 4122
Yu, J., Hekker, S., Bedding, T. R., et al. 2021, MNRAS, 501, 5135
Yu, J., Huber, D., Bedding, T. R., et al. 2016, MNRAS, 463, 1297
Yu, J., Huber, D., Bedding, T. R., et al. 2018, ApJS, 236, 42
Yu, J., Khanna, S., Themessl, N., et al. 2023, ApJS, 264, 41
Zinn, J. C., Stello, D., Huber, D., & Sharma, S. 2019, ApJ, 884, 107